

Chondrule flattening by shock metamorphism in unequilibrated chondrites

Masaaki Miyahara¹, Junnosuke Edanaga¹, Akira Yamaguchi², Takamichi Kobayashi³, Toshimori Sekine⁴, and Ayaka Nakamura¹

¹Hiroshima University

²National Institute of Polar Research

³National Institute for Materials Science

⁴The University of Osaka

November 24, 2022

Abstract

Shock recovery experiments using ALH-78084 H3 and Y-793375 L3 chondrites are conducted in the shock pressure range of 11–43 GPa to reproduce shock-induced melting and chondrule flattening. Shock experiments prove that shock-induced melting occurs beyond 11 GPa at least. The melting occurs at the boundaries between chondrules and matrices. The melts include fine-grained silicate minerals, glasses, and amoeba or spherical metallic Fe-Ni or metallic Fe-Ni-iron-sulfide with a eutectic texture, which coincides with shock-induced melts in shocked natural chondrites. Shock experiments also prove that shock-induced flattening of chondrules occurs and the flattening degree increases with increasing shock pressure. Taking account of not only the shock experiments of ordinary chondrites but also carbonaceous chondrites, the flattening degree does not depend significantly on the densities, porosities, and chondrule/matrix ratios of chondrites. Considering the shock experiments of the Allende CV3 and Murchison CM2 carbonaceous chondrites along with present shock experiments using H/L3 ordinary chondrites, the aspect ratios of chondrules in unequilibrated chondrites (R_{cho}) can be expressed as follows: $R_{\text{cho}} = 0.011 (\pm 1) \times \text{Pressure (GPa)} + 1.18 (\pm 3)$. The long axes of chondrules in shocked ALH-78084 H3 and Y-793375 L3 chondrites have preferred orientations and the degree increases with increasing shock pressure. Natural L/LL3 ordinary chondrites with shock-induced melts have higher aspect ratios and preferred orientations than those without shock-induced melts although it is difficult to determine quantitatively shock pressure using the empirical formula between the aspect ratios of chondrules and shock pressure.

Chondrule flattening by shock metamorphism in unequilibrated chondrites

Masaaki Miyahara^{1*}, Junnosuke Edanaga¹, Akira Yamaguchi², Takamichi Kobayashi³, Toshimori Sekine^{4,5}, and Ayaka Nakamura¹

¹Graduate School of Advanced Science and Engineering, Hiroshima University, Higashi-Hiroshima, 739-8526, Japan

²National Institute of Polar Research, Tokyo 190-8518, Japan

³National Institute for Materials Science, Tsukuba 305-0047, Japan

⁴Center for High Pressure Science and Technology Advanced Research, Pudong, Shanghai 201203, P.R. China

⁵Graduate School of Engineering, Osaka University, Suita, Osaka 565-0871 Japan

*Corresponding author: Dr. Masaaki Miyahara

Graduate School of Advanced Science and Engineering, Hiroshima University, Higashi-Hiroshima, 739-8526, Japan.

Postal code: 739-8526

Telephone: +81-824-24-7461

FAX: +81-82-424-0735

E-mail address: miyahara@hiroshima-u.ac.jp

Key points:

- Shock experiments of H/L3 chondrites were conducted in the range of 11–43 GPa.
- Shock-induced melting occurs above 11 GPa and the aspect ratios of chondrules increase with increasing shock pressure.
- No differences in chondrule flattening between carbonaceous and ordinary chondrites.

Abstract

Shock recovery experiments using ALH-78084 H3 and Y-793375 L3 chondrites are conducted in the shock pressure range of 11–43 GPa to reproduce shock-induced melting and chondrule flattening. Shock experiments prove that shock-induced melting occurs beyond 11 GPa at least. The melting occurs at the boundaries between chondrules and matrices. The melts include fine-grained silicate minerals,

38 glasses, and amoeba or spherical metallic Fe-Ni or metallic Fe-Ni-iron-sulfide with a
39 eutectic texture, which coincides with shock-induced melts in shocked natural
40 chondrites. Shock experiments also prove that shock-induced flattening of
41 chondrules occurs and the flattening degree increases with increasing shock pressure.
42 Taking account of not only the shock experiments of ordinary chondrites but also
43 carbonaceous chondrites, the flattening degree does not depend significantly on the
44 densities, porosities, and chondrule/matrix ratios of chondrites. Considering the
45 shock experiments of the Allende CV3 and Murchison CM2 carbonaceous
46 chondrites along with present shock experiments using H/L3 ordinary chondrites, the
47 aspect ratios of chondrules in unequilibrated chondrites (R_{cho}) can be expressed as
48 follows: $R_{cho} = 0.011 (\pm 1) \times \text{Pressure (GPa)} + 1.18 (\pm 3)$. The long axes of chondrules
49 in shocked ALH-78084 H3 and Y-793375 L3 chondrites have preferred orientations
50 and the degree increases with increasing shock pressure. Natural L/LL3 ordinary
51 chondrites with shock-induced melts have higher aspect ratios and preferred
52 orientations than those without shock-induced melts although it is difficult to
53 determine quantitatively shock pressure using the empirical formula between the
54 aspect ratios of chondrules and shock pressure.

55

56 **Plain Language Summary**

57 An early ordinary chondrite parent-body had an onion-shell structure and was
58 disrupted by an impact. Some ordinary chondrites derived from the parent-body
59 surface have melts, high-pressure polymorphs, and flattened chondrules, which may
60 be due to shock metamorphism. Hence, shock recovery experiments using ordinary
61 chondrites were conducted in the shock pressure range of 11–43 GPa to reproduce
62 shock-induced melting and chondrule flattening. Shock-induced melting occurs
63 beyond 11 GPa. The melting occurs at a boundary between chondrules and
64 surrounding fine-grained materials. Shock-induced flattening of chondrules occurs
65 and the flattening degree increases with increasing shock pressure. Taking account of
66 not only the shock experiments of ordinary chondrites but also carbonaceous
67 chondrites, the flattening degree does not depend significantly on the densities,
68 porosities, and chondrule/matrix ratios of chondrites. The aspect ratios of chondrules
69 in unequilibrated chondrites (R_{cho}) can be expressed as follows: $R_{cho} = 0.011 (\pm 1)$
70 $\times \text{Pressure (GPa)} + 1.18 (\pm 3)$. The long axes of chondrules in experimentally shocked
71 ordinary chondrites have preferred orientations and the degree increases with
72 increasing shock pressure.

73

74 **1. Introduction**

75 One of the classic structure models for ordinary chondrite parent-bodies is the
76 onion shell model derived from maximum metamorphic temperature and cooling rate
77 recorded in each petrologic type ordinary chondrite (e.g., Trierhoff et al., 2003).
78 Following the onion shell model, early ordinary chondrite parent-bodies had
79 consisted of petrologic type 3–6 ordinary chondrites toward the inside from the
80 outside. The early ordinary chondrite parent-bodies were disrupted by impacts and
81 the fragments escaped from the parent-bodies.

82 Shock features recorded in ordinary chondrites have been investigated to clarify
83 the disruption histories. Most works have focused on petrologic type 5 and 6
84 ordinary chondrites derived from the inner portions of the parent-bodies (e.g., Chen
85 et al., 1996; Ohtani et al., 2004). In contrast, few works have worked on shock
86 features recorded in petrologic type 3 and 4 ordinary chondrites derived from the
87 outer portions of the parent-bodies (Ruzicka et al., 2015a–b), because, in general, the
88 shock features in petrologic type 3 and 4 ordinary chondrites are not distinct
89 compared to those in petrologic type 5 and 6 ordinary chondrites.

90 Miyahara et al. (2021) conduct systematic investigations of shock-induced melts
91 and high-pressure polymorphs in ordinary chondrites and report that some petrologic
92 type 3 ordinary chondrites have shock-induced melts and high-pressure polymorphs.
93 Also, some petrologic type 3 ordinary chondrites with shock-induced melts include
94 flattened chondrules. Foliation in chondrites is formed during the sedimentation of
95 chondrules on the parent-bodies (Dodd, 1965; Martin & Mills, 1980). The foliation
96 in chondrites also can be formed by impacts because when a shock wave propagates
97 in a rock, uniaxial compaction occurs (Sneyd et al., 1998; Gattacceca et al., 2005).

98 We raise the possibility that the flattened chondrules in type 3 ordinary chondrites
99 are due to shock metamorphism and the aspect ratios of chondrules depend on shock
100 pressure. Several shock recovery experiments using equilibrated ordinary chondrites
101 were conducted to clarify the shock features (e.g., Stöffler et al., 1991; Kohout et al.,
102 2020). In contrast, shock recovery experiments using unequilibrated ordinary
103 chondrites have not been conducted so far.

104 The average size of chondrules in H3 chondrites is distinct from those of L/LL3
105 chondrites: the mean diameters of chondrules in H3 and L/LL3 are about 450 and
106 500–550 μm , respectively (Friedrich et al., 2015). The flattening degree of
107 chondrules may depend on the size distribution of chondrules. Hence, we conduct
108 shock recovery experiments using H3 and L3 chondrites to i) reproduce
109 shock-induced melt and chondrule flattening and ii) clarify the relationship between
110 flattening degree and shock pressure. This study also uses several Antarctic and
111 non-Antarctica petrologic type 3 ordinary chondrites with or without a

112 shock-induced melt to verify the shock recovery experiments.

113

114 **2. Materials and experimental methods**

115 **2.1 Materials**

116 Shock experiments used two petrologic-type 3 ordinary chondrites: the Allan
117 Hills (ALH)-78084 H3 and Yamato (Y)-793375 L3. Sliced ALH-78084 H3 (Area:
118 about 20 x 40 mm², thickness: about 2.73 mm) and Y-793375 L3 (Area: about 22 x
119 38 mm², thickness: about 2.08 mm) samples were allocated from the National
120 Institute of Polar Research (NIPR), Japan. These two chondrites show a
121 well-preserved chondritic texture suitable as starting materials for the shock
122 experiments. Fifteen H3, twenty-three L3, and twenty-three LL3 ordinary chondrites
123 were selected for the comparisons and verifications of the shock recovery
124 experiments. The classification of individual samples (chemical group and petrologic
125 type) followed the Meteoritical Society Bulletin database.

126 **2.2 Shock experiments**

127 The allocated ALH-78084 H3 and Y-793375 L3 chondrite samples were
128 adhered to glasses using CrystalbondTM 509. Doubly polished samples with a
129 thickness of 1.5 mm were made by a surface grinding machine. Disc samples (ϕ = 6
130 or 12 mm) were cored out from the doubly polished samples by an ultrasonic
131 machine. The cored-out disc samples were put in acetone for thirty hours to remove
132 CrystalbondTM and dried at 373 K for thirty hours. The prepared disc samples were
133 kept in a closed plastic bag with a silica gel until shock experiments.

134 The densities of individual disc samples were calculated by measuring their
135 thicknesses, diameters, and weights (Table 1). The disc samples were put into
136 stainless (SUS 304) containers (30 mm diameter x 30 mm long). The disc samples
137 were placed at a depth of 3 mm from the impact surface of the stainless container.
138 Shock experiments used a 30-mm bore propellant gun installed at the National
139 Institute for Materials Science (NIMS), Tsukuba, Japan. 2-mm thick steel (SUS 304)
140 or tungsten (W) flyer plate, attached to the head of a projectile, impacted the stainless
141 containers. Velocity just before the impact was measured with a magneto flyer
142 method (Kondo et al., 1977). The peak shock pressure was calculated by the
143 impedance match method assuming the sample pressure reached equilibrium with the
144 container pressure because the experimental procedures are similar to those
145 described by Yamaguchi & Sekine (2000). Table 1 shows the details of individual
146 experimental conditions.

147 **2.3 Sample analysis**

148 Stainless containers were recovered after individual shock experiments and were

149 sliced open with a diamond saw and lathe to observe the cross-sections of disc
150 samples. 1-3 slices were made from each recovered stainless container. The slices
151 were embedded into an epoxy resin and were polished with an abrasive paper under
152 the dry condition to reduce the exfoliation of the disc samples.

153 We took back-scattered electron (BSE) images of polished cross-sections by a
154 field-emission scanning electron microscope (FE-SEM): JEOL JSM-7100F (installed
155 at NIPR) at an accelerating voltage of 15 kV. A dedicated image processing
156 application the Oxford AZtec installed in JEOL JSM-7100F combined all individual
157 BSE images into one BSE image depicting the whole area of the cross-section.
158 Subsequently, individual melts and deformation textures in the cross-sections were
159 observed under higher magnification BSE image mode. The short and long axes of
160 chondrules in the cross-sections were measured using the combined BSE images and
161 dedicated image processing application SmartGrain (Tanabata et al., 2012). The
162 measured axis lengths are apparent. The measured axis lengths (2D) were converted
163 to the actual lengths (3D) by multiplying a factor of 1.273 (Kong et al., 2005). The
164 angles of the long axes to an arbitrary axis were measured by the image processing
165 application ImageJ. The total lengths of open cracks in individual cross-sections
166 were also measured by ImageJ.

167 The whole area BSE images of selected petrologic type 3 ordinary
168 chondrites were also observed by FE-SEM to measure the short and long axes of
169 chondrules and the angles of the long axes to an arbitrary axis. Individual melts and
170 deformation textures were observed under higher magnification BSE image mode.
171 The measurement procedures of the chondrules are as same as the samples recovered
172 after shock experiments. The mineralogy of melts was determined using a laser
173 micro-Raman spectrometer: Renishaw inVia (at NIPR). An optical microscope was
174 used to focus the excitation laser beam (the 532 nm line of green laser). The laser
175 power was kept at $< \sim 7$ mW to reduce laser beam damage. The acquisition time was
176 10–60 s. For each phase, the Raman spectrum was acquired in the spectral region of
177 200 to 1500 cm^{-1} .

178

179 **3. Results**

180 **3.1 Petrologic descriptions of starting materials**

181 Figures S1–2 show the petrologic thin sections of unshocked ALH-78084 H3 and
182 Y-793375 L3 chondrites. No distinct shock features such as undulatory extinction
183 and fractures were observed in the petrologic thin sections. Figures S3a–b show the
184 representative petrological textures of ALH-78084 H3 and Y-793375 L3 chondrites,

185 respectively. Melts were not found in ALH-78084 H3 and Y-793375 L3 chondrites.
186 A small amount of weathering vein occurred in ALH-78084 H3 chondrite (Fig. S3a).

187 The long and short axes of chondrules in ALH-78084 H3 and Y-793375 L3
188 chondrites were measured using the petrologic thin sections. The distributions of
189 long and short axes did not follow the Gaussian distribution (Figs. S4a–d). The long
190 and short axes of chondrules in ALH-78084 H3 chondrite were respectively 429 μm
191 and 352 μm (median, $n = 258$) (Table 2). Those in Y-793375 L3 chondrite were 773
192 μm and 634 μm ($n = 143$) (Table 2). The aspect ratios of chondrules in ALH-78084
193 H3 and Y-793375 L3 chondrites were respectively 1.19 and 1.22 (median) (Figs.
194 S4e–f, Table 2). The number densities of chondrules in ALH-78084 H3 and
195 Y-793375 L3 chondrites were 2.12 and 1.18 mm^{-2} .

196 **3.2 Experimentally shocked ALH-78084 H3 chondrite**

197 Shock experiments were conducted in the shock pressure range from 11 to
198 43 GPa (Table 1). Six samples were successfully recovered after shock experiments.
199 Three polished slices were prepared from each recovered sample except for Shot No.
200 H_7. Figure S5 shows the whole area BSE images depicting the cross-sections of
201 recovered samples. Some recovered samples were concave in the shapes. With
202 increasing shock pressure, the degree of concave became bigger (Fig. S5). A part of
203 sample Shot No. H_6 (42.9 GPa) came out into the stainless container (Fig. S5e).
204 Open cracks cutting chondrules occurred in most samples and arranged sub-parallel
205 to shockwave front (Figs. 1a, S5). Figure 2a shows the drawing of open cracks in
206 each shot. The length of open cracks per unit square in each shot is shown in Table 2.

207 Some olivine grains in shocked samples had irregular and/or planar fractures
208 (Fig. 1b). Melts were found from all the shocked samples. Melts occurred along
209 boundaries between chondrules and matrices consisting of fine-grained materials
210 (Fig. 1c). In most cases, each melt was isolated and not interconnected with each
211 other. The melts consisted of quenched melts and mineral and/or chondrule
212 fragments. The quenched melts consisted of fine-grained silicate minerals (olivine
213 and pyroxene), glasses, and metals (Fig. 1d). The mineral and chondrule fragments
214 entrained in the melts were rounded due to melting (Fig. 1d). The metals, which were
215 in the shapes of amoeba or spherule, consisted of metallic Fe-Ni or metallic Fe-Ni–
216 iron-sulfide with a eutectic texture (Figs. 1d–f). Voids occurred in the melts (Figs.
217 1e–f). No high-pressure polymorphs were found from the quenched melts or mineral
218 and/or chondrule fragments.

219 The long and short axes of chondrules and chondritic fragments in the
220 shocked samples were measured. The aspect ratios are shown in Table 2 and Figure
221 3a. The number of measurable chondrules decreased with increasing shock pressure

because the deformation degree of sample containers increased (Fig. S5). All the aspect ratios of chondrules in the shocked samples (1.19–1.57) were bigger than that of starting material (1.19)(Table 2). Azimuths of long axes to an impact surface were measured (Table S1, Fig. S6). Chondrules in Shot No. H_7 were not measured because its cross-section was too small for measurements. Only textural observations by FE-SEM were conducted for Shot No. H_7.

3.3 Shocked Y-793375 L3 chondrite

Shock experiments were conducted in the shock pressure range from 11 to 43 GPa for Y-793375 L3 (Table 1). Six samples were successfully recovered after shock experiments. Three polished slices were prepared from each recovered sample. Figure S7 shows the whole area BSE images depicting the cross-sections of recovered samples. Some recovered samples were concave in the shapes and the degree became bigger with increasing shock pressure (Figs. 2b, S7). A part of sample Shot No. L_6 (42.5 GPa) came out into the stainless container (Fig. S7f). Open cracks arranging sub-parallel to shockwave occurred in the shocked samples (Fig. 4a). Figure 2b shows the drawings of open cracks in each shot. The length of open cracks per unit square in each shot is shown in Table 2.

Some olivine grains in shocked samples had irregular and/or planar fractures (Fig. 4b). Melts were found from all the shocked samples. Isolated melting occurred along with boundaries between chondrules and matrices (Fig. 4c). The textures and constituents of melts were similar to those of ALH-78084 H3 chondrite (Figs. 4c–f). Some melted chondrule glasses had a flow-like texture (Fig. 4e). One-third of the cross-section of Shot No. L_4 (26.4 GPa) was melted (Figs. S7d, S8a). The quenched melts consisted mainly of fine-grained pyroxene with a dendrite texture, glasses, and metallic Fe-Ni-FeS with a eutectic texture (Figs. S8b–c). Voids occurred in the glasses and also in some metals (Fig. S8c). No high-pressure polymorphs were found from all the shocked samples.

The long and short axes of chondrules (and chondritic fragments) and the aspect ratios in the shocked samples are shown in Table 2. All the aspect ratios of shocked samples (1.36–1.75) were bigger than that of starting material (1.22)(Table 2). The azimuths of long axes to an impact surface are shown in Table S1 and Figure S9.

3.4 Petrologic type 3 ordinary chondrites

Shock-induced melts and aspect ratios of chondrules (and chondritic fragments) in selected H/L/LL3 ordinary chondrites were investigated. Typical whole area BSE images of investigated H/L/LL3 ordinary chondrites are shown in Figure S10. The modes of melting are shown in Tables S2–4 and the definition of

melting followed Miyahara et al. (2021): i) pocket, ii) line, and iii) network. The textures and constituents of shock-induced melts were similar to those of shocked ALH-78084 H3 and Y-793375 L3 chondrites (Figs. 5a–b). Melting occurred also in some fragments of chondrule glasses in contact with the shock-induced melts (Figs. 5c–d). Void, which was ubiquitously observed in shocked ALH-78084 H3 and Y-793375 L3 chondrites, did not occur in the shock-induced melts of H/L/LL3 ordinary chondrites. Distinct open cracks cutting chondrules, which was observed in shocked ALH-78084 H3 and Y-793375 L3 chondrites, were not observed in H/L/LL3 ordinary chondrites. By contrast, open cracks occurred in the shock-induced melts of some L/LL3 ordinary chondrites (Fig. 5e).

The long and short axes of chondrules (and chondritic fragments) in H/L/LL3 chondrites are shown in Tables S2–4. In fifteen H3 chondrites, only Y-981139 H3 chondrite included a shock-induced melt (Table S2). No high-pressure polymorphs occurred in Y-981139 H3 chondrite. The difference in the aspect ratios between H3 ordinary chondrites without (1.17–1.28) or with shock-induced melts (1.24) was not clear (Fig. 6, Table S2). In twenty-three L3 chondrites, sixteen L3 chondrites included shock-induced melts (Table S3). Y-981327 chondrite had a pervasive shock-induced melt (Figs. S10b–c). Asuka (A)-880870, A-881096, Y-86706, and Northwest Africa (NWA) 8664 L3 chondrites included Na-pyroxene and coesite as high-pressure polymorphs (Figs. 5e–f, Table S3). The aspect ratios of chondrules in L3 ordinary chondrites without or with shock-induced melts were 1.20–1.36 and 1.27–1.75, (Table S3). The aspect ratio of chondrules in Y-981327 chondrite was higher (1.75) than others (Table S3, Fig. 7). In twenty-three LL3 ordinary chondrites, five LL3 ordinary chondrites included shock-induced melts (Table S4, Fig. 8). A-881199 and A-881981 LL3 chondrites included Na-pyroxene and coesite as high-pressure polymorphs. The aspect ratios of chondrules in LL3 ordinary chondrites without or with shock-induced melts were 1.16–1.41 and 1.31–1.54 (Table S4). The angles of long axes to arbitrary axes in H/L/LL3 ordinary chondrites were also measured (Tables S2–4).

288

289 **4. Discussion**

290 **4.1 shock-induced melting**

Melting occurs in all the shocked ALH-78084 H3 and Y-793375 L3 chondrite samples and the melts have evidence of immiscibility between silicate melts and metallic melts under high-pressure (e.g., Kato & Ringwood, 1989). The melts in the shocked samples consist of fine-grained silicate minerals (olivine and/or pyroxene), glasses, and the spherules of metallic Fe-Ni or metallic Fe-Ni–

295

296 iron-sulfide with a eutectic texture (Figs. 1c–f, 4c–d). Some spherules of fine-grained
297 silicate mineral assemblages are included in the spherules of metallic Fe-Ni or
298 metallic Fe-Ni-iron-sulfide with a eutectic texture (Figs. 1c–d, 4f). All these features
299 indicate that melting occurs under high-pressure.

300 The temperature in the shocked ALH-78084 H3 and Y-793375 L3 chondrite
301 samples during the impact is not homogeneous. Most chondrules in shocked samples
302 do not show clear evidence of melting (Figs. S5, S7). Melting occurs in matrices in
303 contact with chondrules (Figs. 1c, 4c). The porosity of matrices is higher compared
304 to that of chondrules because the matrices are fine-grained crystal assemblages.
305 When compression wave propagates in un-equilibrated chondrites, their matrices
306 with relatively low shock impedance decrease their volumes more drastically than
307 their chondrules with relatively high shock impedance. The large volume decrease
308 induces a temperature spike resulting in local melting in the matrices.

309 The petrologic structure of un-equilibrated chondrites, which consists of
310 coarse-grained chondrules and fine-grained materials (matrices), makes
311 shock-induced melting easier under low pressure. Hirata et al. (2009) conducted
312 shock experiments using mimic porous primitive chondritic materials (initial
313 porosity: $35\pm 5\%$). Shock veins occur above 25 GPa in the shocked mimic porous
314 primitive chondritic materials. By contrast, shock-induced melting occurs in the
315 un-equilibrated H3 and L3 ordinary chondrites with low porosities even at 11 GPa. A
316 local temperature spike under low shock pressure in un-equilibrated chondrites is
317 predicted by numerical simulation (Bland et al., 2014). The petrologic structure of a
318 target becomes a more important factor in some cases than its porosity for
319 shock-induced melting.

320 If petrologic type 3 ordinary chondrites expose on asteroids, the surfaces
321 have experienced melting along with brecciation. The onion shell model proposes
322 that petrologic type 3 ordinary chondrites have made up the outmost layers of
323 ordinary chondrite parent-bodies (e.g., Tieloff et al., 2003). Shock experiments
324 prove that even if the impact of 0.57 km/sec causes shock-induced melting in
325 petrologic type 3 ordinary chondrites. Following the Rankine-Hugoniot equation,
326 shock pressure depends on impact velocity. In general, the existence of
327 shock-induced melts in ordinary chondrites implies high shock pressure. However,
328 petrologic type 3 ordinary chondrites do not apply the criterion. The impact velocity
329 of 0.57 km/sec is much lower compared to the most probable impact velocity in the
330 asteroid belt (4.4 km/sec) (Bottke et al., 1994). The surfaces of S-type asteroids may
331 like lunar regolith that includes brecciated rocks and melts.

332 Heating by shock-induced melts does not significantly affect thermal
333 metamorphism in petrologic type 3 ordinary chondrites. Numerical simulations
334 indicate that the temperature of matrices during the impact becomes higher with
335 increasing chondrule/matrix ratios at the same impact speed in unequilibrated
336 chondrites (Bland et al., 2014). The maximum temperature in petrologic type 3
337 ordinary chondrites is higher compared to carbonaceous chondrites because the
338 former includes a few amounts of matrices (Weisberg et al., 2006). The
339 shock-induced melts in the matrices may work as a heat source for thermal
340 metamorphism. However, the heat sources in the petrologic type 3 ordinary
341 chondrites are small due to the limited amounts of matrices. Hence, the
342 shock-induced melts do not affect the bulk-rock temperature of petrologic type 3
343 ordinary chondrites.

344 Voids occur in the shock-induced melts of shocked ALH-78084 H3 and
345 Y-793375 L3 chondrite samples (Figs. 1f, 4f), which is due to the degassing of
346 volatile elements during the decompression stage. Parts of shocked chondrites melt,
347 and volatile elements are dissolved into the melts under high-pressure. The degassing
348 occurs before the melts are quenched. Decompression is initiated when a rarefaction
349 wave catches up the compression wave. Assuming that the longitudinal wave
350 velocities of chondrite and stainless container at ambient pressure conditions are 6
351 and 5.77 km/sec., respectively, the propagations of compression and rarefaction
352 waves in the sample containers are calculated. The rarefaction wave achieves the
353 backside of samples in 1–2 μ sec after the impact. The quenching of melts is initiated
354 by thermal conduction into the stainless container. The degassing is due to the
355 limited duration of high-pressure compared to the time required for the quenching.

356 Shock-induced melts in investigated H/L/LL3 chondrites do not include
357 voids (Fig. 5), which is due to the difference in the durations of high-pressure
358 between shock experiments and natural impact events. The duration of high-pressure
359 recorded in several ordinary chondrites is estimated using the kinetics of
360 high-pressure polymorphs or diffusion rates of trace elements (Ohtani et al., 2004;
361 Beck et al., 2005; Xie et al., 2006). The durations (several milliseconds to seconds)
362 are much longer than the shock experiments (several microseconds). Hence, the
363 melts can be quenched under high-pressure.

364 Some quenched melts include fractures (Figs. 5e–f), which is due to a
365 heterogeneous compression in un-equilibrated chondrites. The quenched melts,
366 which are quenched under high-pressure after melting, is denser than original
367 matrices. Chondrules are less compacted due to low porosity during the compression

stage. The fractures in the melts are induced by the tensile failure of the quenched melts during the decompression stage.

4.2 Shock-induced flattening of chondrules

The aspect ratios of chondrules in shocked ALH-78084 H3 and Y-793375 L3 chondrites increase with increasing shock pressure (Fig. 3c), indicating that the chondrules are deformed by shock metamorphism. Shock recovery experiments prove that both the chondrule flattening along with melting occur in type 3 ordinary chondrites by shock metamorphism. Linear fitting is conducted for plotted data by the least-squares method (Fig. 3c). The aspect ratios at ambient pressure are fixed with the aspect ratios of chondrules in starting materials. The calculated slopes for ALH-78084 H3 and Y-793375 L3 chondrites are 0.88×10^{-2} and 1.09×10^{-2} . The aspect ratios of chondrules in experimentally shocked Murchison CM2 and Allende CV3 chondrites (Tomeoka et al., 1999; Nakamura et al., 2000) are also plotted in Figure 3c. The calculated slopes for Murchison CM2 and Allende CV3 chondrites are 1.40×10^{-2} and 2.38×10^{-2} .

Considering the interquartile range, the flattening degree of chondrules in Y-793375 L3 chondrite is a bit higher than that in ALH-78084 H3 chondrite (Figs. 3a–c), which is due to the grain refining of chondrules. There are no distinct differences in the densities and chondrule/matrix ratios between ALH-78084 H3 and Y-793375 L3 chondrites as starting materials (Table 1). By contrast, the size of chondrules in ALH-78084 H3 chondrite is finer than that of Y-793375 L3 chondrites (Table 1). A petrologic-type 3 ordinary chondrite is an assemblage of chondrules, which can be regarded as a polycrystal. Yield stress (σ_y) can be described by the Hall-Petch relationship,

$$\sigma_y = \sigma_0 + k_y d^{-1/2}$$

where σ_0 , k , and d are the internal stress, the strengthening coefficient, and grain size, respectively. Following the Hall-Petch relationship, the yield stress of petrologic type 3 ordinary chondrites increases with decreasing the size of chondrules. The strengthening by grain refinement inhibits the flattening of chondrules in ALH-78084 H3 chondrite.

The size sorting of chondrules also affects the flattening degree of chondrules. The size of chondrules in ALH-78084 H3 chondrite is sorted, whereas that in Y-793375 L3 chondrite is scattered (Fig. S4). In petrologic type 3 ordinary chondrites consisting of chondrules with varied sizes, the yield stress is heterogeneous. The heterogeneous yield stress decreases the strength of Y-793375 L3 chondrite as a bulk-rock, which increases the flattening degree of chondrules.

404 The relative abundance of matrices (+ lithic or mineral fragments) does not
405 significantly affect the flattening degree of chondrules. The relative abundances of
406 chondrules and matrices (+ lithic or mineral fragments) in Allende CV3 chondrites
407 are 35–43 % and 41–55 % (McSween, 1977; Ebel et al., 2016). Those in Murchison
408 CM2 are ~16 % and ~75 % (McSween, 1979). The relative abundances of
409 chondrules in ALH-78084 H3 (chondrule: 65 %, matrix: 15 %) and Y-793375 L3
410 (chondrule: 63 %, matrix: 23 %) chondrites are much higher than Murchison CM2
411 and Allende CV3 chondrites. However, the flattening degree of chondrules in
412 Murchison CM2 chondrite is similar to those of ALH-78084 H3 and Y-793375 L3
413 chondrites.

414 A bulk-rock porosity does not also affect the flattening degree of chondrules.
415 The porosities of Allende CV3 and Murchison CM2 are 16.9–27.9 % and 18.8–
416 24.9 % (Macke et al., 2011). Although the porosities of ALH-78084 H3 and
417 Y-793375 L3 chondrites are not measured, the average porosities of H and L
418 ordinary chondrites are 7.0 and 5.6 % (Consolmagno et al., 2008). However, there
419 are no distinct differences in the flattening degrees between H/L3 ordinary chondrites
420 and Murchison CM2 chondrite. The flattening degree of chondrules in Allende CV3
421 chondrite is much higher than Murchison CM2 chondrite although there are no
422 distinct differences in their physical properties (Fig. 3c). We could not find an
423 adequate factor to explain the difference.

424 Long axes of flattened chondrules have a weak preferred orientation because
425 of uniaxial compression during shock metamorphism. The long axes of chondrules in
426 ALH-78084 H3 and Y-793375 L3 chondrites do not arrange homogeneously (Figs.
427 S6, S9). We first draw the Lorenz curves using the azimuths of long axes in starting
428 materials and each shocked sample (Table S1, Figs. S11a–b) and calculate the Gini
429 coefficients to evaluate the preferred orientation (Table 2). The Gini coefficients of
430 long axes in ALH-78084 H3 and Y-793375 L3 chondrites as starting materials are
431 0.33 and 0.32, respectively (Table 2). If the long axes do not have preferred
432 orientations, the Gini coefficient becomes null. Although the Gini coefficients of
433 ALH-78084 H3 and Y-793375 L3 chondrites keep small, the values become bigger
434 slightly with increasing shock pressure (Fig. S11c).

435 Open cracks in shocked samples are induced by tensile failure when
436 compressive stress is reflected at the free surface of a stainless container and
437 becomes tensile stress. The lengths of open cracks in shocked ALH-78084 H3 and
438 Y-793375 L3 chondrites increase with increasing shock pressure (Fig. 3d). However,
439 the linear relationship between shock pressure and lengths is not clear. It is difficult
440 to adopt the relationship for the estimation of shock pressure.

441 **4.3 Estimation of shock pressure by aspect ratios of chondrules**

442 The shock pressure recorded in each H/L/LL3 ordinary chondrite is
443 estimated using by adopting the aspect ratios of chondrules (median) into the
444 empirical formulae obtained from shock experiments to estimate shock pressure
445 (Tables S2–4). The empirical formulae obtained from ALH-78084 H3 and Y-793375
446 L3 chondrites are adopted for H3 and L/LL3 ordinary chondrites, respectively.
447 Figures 6–8 show box plots showing the aspect ratios of chondrules in each H/L/LL3
448 ordinary chondrite and estimated shock pressure. The ordinary chondrites in each
449 figure are sorted according to the aspect ratios.

450 No difference is found in estimated shock pressure between H3 ordinary
451 chondrites with a shock-induced melt (Gray-colored box) or without a shock-induced
452 melt (White-colored melt) (Fig. 6). The estimated shock pressure of Y-981139 H3
453 chondrite with a shock-induced melt is 4.8 GPa (Table S2). The estimated shock
454 pressure of H3 ordinary chondrites without shock-induced melts is up to about 10
455 GPa. Several estimated shock pressure values are below zero, which is impossible.

456 By contrast, the estimated shock pressure of L/LL3 ordinary chondrites with
457 shock-induced melts is higher than those of L/LL3 ordinary chondrites without
458 shock-induced melts (Tables S3–4, Figs. 7–8). The estimated shock pressure of L3
459 ordinary chondrites without shock-induced melts is less than 7.8 GPa except for
460 A-881244 L3 chondrite. The estimated shock pressure of most L3 ordinary
461 chondrites with shock-induced melts is higher than 7.8 GPa. The chondrules of
462 Y-981327 L3 chondrite have a very high aspect ratio (1.75) and the estimated shock
463 pressure is also very high (48.2 GPa)(Table S3). Y-981327 L3 chondrite is heavily
464 shocked because it has the extensive shock-induced melts (Figs. S10b–c).

465 No obvious correlation is found between estimated shock pressure and
466 high-pressure polymorphs (Tables S3–4). No wonder that there is no correlation
467 among shock pressure estimated from the aspect ratios of chondrules, shock-induced
468 melts, and high-pressure polymorphs. The formations of high-pressure polymorphs
469 are controlled by kinetics. Even if both high-pressure and -temperature conditions
470 required for the formation of high-pressure polymorphs are achieved, high-pressure
471 polymorphs cannot form if their duration is not enough. It is also possible that
472 high-pressure polymorphs, which formed during compression and equilibrium stages
473 once, back-transforms into their low-pressure polymorphs during the subsequent
474 adiabatic decompression stage if the cooling is slow.

475 Some estimated shock pressure values are invalid, which is due to the
476 deviation of aspect ratios of intact chondrules that are free from shock
477 metamorphism. The mean aspect ratio of intact chondrules in LL3 chondrites is $1.2 \pm$

0.18 ($n = 719$) (Nelson & Rubin, 2002), which coincides with the aspect ratios of chondrules (and chondritic fragments) in ALH-78084 H3 and Y-793375 L3 chondrites as starting materials (Table 2). Considering the standard deviation, in the case of less shocked ordinary chondrites, some shock pressure values estimated from the aspect ratios of chondrules becomes invalid. In contrast, some estimated shock pressure values become overestimated.

The preferred orientations of long axes of chondrules become distinct in highly shocked L/LL3 chondrites, especially including shock-induced melts (Tables S2–4, Fig. S12). The Gini coefficients increase with increasing shock pressure in L/LL3 chondrites. The L/LL3 chondrites including shock-induced melts have higher Gini coefficients than those without melts. The degrees of preferred orientations in L/LL3 chondrites are higher compared to those of experimentally shocked chondrites. The variance is due to the differences in the duration of compression between shock experiments and natural impacts although all impacts in nature do not have long compression time.

To conclude, it is difficult to use the aspect ratios of chondrules for the quantitative estimation of shock pressure in petrologic type 3 ordinary chondrites. Repeated low-velocity impacts may increase the aspect ratios of chondrules gradually, which is proved by the shock experiments of Allende CV3 chondrite (Nakamura et al., 2000). The aspect ratios of chondrules in pre-heated Allende CV3 chondrite become bigger than those of chondrules at room temperature. Ordinary chondrite parent-bodies had a heat source such as ^{26}Al when they were born. If impacts occur on hot parent-bodies, the flattening degree of chondrules becomes bigger than that of chondrules on cold parent-bodies. Although chondrules with a high aspect ratio and preferred orientation become a screening standard for strong shock metamorphism, it does not work as a quantitative shock pressure barometer.

504

505 **5. Conclusions**

- 506 1) Shock experiments using ALH-78084 H3 and Y-793375 L3 chondrites prove
507 that shock-induced melting occurs in petrologic type 3 chondrites beyond 11
508 GPa at least. The melting occurs at boundaries between chondrules and matrices.
- 509 2) Shock-induced flattening of chondrules occurs in petrologic type 3 chondrites.
510 The flattening degree increases with increasing shock pressure.
- 511 3) There is no significant difference in the flattening degree of chondrules between
512 carbonaceous and ordinary chondrites. The flattening degree does not depend
513 significantly on the densities, porosities, and chondrule/matrix ratios of
514 chondrites. Finally, by considering the relationships between the aspect ratios of

515 chondrules and shock pressure in carbonaceous and ordinary chondrites, the
 516 aspect ratios in unequilibrated chondrites (R_{cho}) can be expressed following the
 517 linear equation: $R_{cho} = 0.011 (\pm 1) \times \text{Pressure (GPa)} + 1.18 (\pm 3)$.
 518 4) The long axes of chondrules have a preferred orientation and the degree
 519 increases with increasing shock pressure.
 520 5) Natural L/LL3 ordinary chondrites with shock-induced melts have higher aspect
 521 ratios and preferred orientations of chondrules than those without shock-induced
 522 melts.
 523 6) It is difficult to determine quantitatively shock pressure in petrologic type 3
 524 chondrites using the empirical formula between the aspect ratios of chondrules
 525 and shock pressure.

526

527 **Acknowledgments**

528 This study was supported by Grants-in-Aid for Scientific Research, no. 18H01269
 529 from the Ministry of Education, Culture Sports, Science, and Technology (MEXT) to
 530 M.M. This study was also financially supported by NIPR through General
 531 Collaboration Projects nos. 26-31 and KP-307. We acknowledge Dr. M. Kayama for
 532 providing the design drawing of a sample container used in this shock experiment.
 533 The measured aspect ratios and azimuth of chondrules are available in Miyahara
 534 (2021).

535

536 **References**

537 Beck P., Gillet Ph., El Goresy A., & Mostefaoui S. (2005). Timescales of shock
 538 processes in chondritic and martian meteorites. *Nature* 435, 1071–1074.
 539 Bland P.A., Collins G.S., Davison T.M., Abreu N.M., Ciesla F.J., Muxworthy A.R., &
 540 Moore J. (2014). Pressure–temperature evolution of primordial solar system solids
 541 during impact-induced compaction. *Nature Communications* 5, 5451 doi:
 542 10.1038/ncomms6451.
 543 Bottke Jr. W.F., Nolan M.C., Greenberg R., & Kolvoord R.A. (1994). Velocity
 544 distributions among colliding asteroids. *Icarus* 107, 255–268.
 545 Chen M., Sharp T.G., El Goresy A., Wopenka B., & Xie X. (1996). The
 546 majorite-pyroxene + magnesiowüstite assemblage: Constraints on the history of
 547 shock veins in chondrites. *Science* 271, 1570–1573.
 548 Consolmagno G.J., Britt D.T., & Macke R.J. (2008). The significance of meteorite
 549 density and porosity. *Chemie der Erde* 68, 1–29.
 550 Dodd Jr. R.T. (1965). Preferred orientation of chondrules in chondrites. *Icarus* 4,
 551 308–316.

552 Ebel D.S., Brunner C., Konrad K., Leftwich K., Erb I., Lu M., Rodriguez H., Ellen J.
 553 Crapster-Pregont E.J., Friedrich J.M., & Weisberg M.K. (2016). Abundance,
 554 major element composition and size of components and matrix in CV, CO and
 555 Acfer 094 chondrites. *Geochimica et Cosmochimica Acta* 172, 322–356.
 556 Friedrich J.M., Weisberg M.K., Ebel D.S., Biltz A.E., Corbett B.M., Iotzov I.V.,
 557 Khan W.S., & Wolman M.D. (2015). Chondrule size and related physical
 558 properties: A compilation and evaluation of current data across all meteorite
 559 groups. *Chemie der Erde* 75, 419–443.
 560 Gattacceca J., Rochette P., Denise M., Consolmagno G., & Folco L. (2005). An
 561 impact origin for the foliation of chondrites. *Earth and Planetary Science Letters*
 562 234, 351–368.
 563 Hirata N., Kurita K., & Sekine T. (2009). Simulation experiments for shocked
 564 primitive materials in the Solar System. *Physics of the Earth and Planetary*
 565 *Interiors* 174, 227–241.
 566 Kato T. & Ringwood A.E. (1989). Melting relationships in the system Fe-FeO at high
 567 pressures: Implications for the composition and formation of the earth's core.
 568 *Physics and Chemistry of Minerals* 16, 524–538.
 569 Kondo K.I., Sawaoka A., & Saito S. (1977). Magneto flyer method for measuring
 570 gas-gun projectile velocities. *Review of Scientific Instruments* 48, 1581–1582.
 571 Kong M., Bhattacharya R.N., James C., & Basu A. (2005). A statistical approach to
 572 estimate the 3D size distribution of spheres from 2D size distributions. *Geological*
 573 *Society of America Bulletin* 117, 244–249.
 574 Kohout T., Petrova E.V., Yakovlev G.A., Grokhovsky V.I., Penttilä A., Maturilli A.,
 575 Moreau J.G., Berzin S.V., Wasiljeff J., Danilenko I.A., Zamyatin D.A.,
 576 Muftakhetdinova R.F., & Heikkilä M. (2020). Experimental constraints on the
 577 ordinary chondrite shock darkening caused by asteroid collisions. *Astronomy &*
 578 *Astrophysics*, doi: <https://doi.org/10.1051/0004-6361/202037593>.
 579 Martin P.M. & Mills A.A. (1980). Preferred chondrule orientations in meteorites.
 580 *Earth and Planetary Science Letters* 51, 18–25.
 581 Macke R.J., Consolmagno G.J., & Britt D.T. (2011). Density, porosity, and magnetic
 582 susceptibility of carbonaceous chondrites. *Meteoritics and Planetary Science* 46,
 583 1842–1862.
 584 McSween Jr. H.Y. (1977). Petrographic variations among the carbonaceous
 585 chondrites of the Vigarano type. *Geochimica et Cosmochimica Acta* 41, 1777–
 586 1790.
 587 McSween Jr. H.Y. (1979). Alteration in CM carbonaceous chondrites inferred from
 588 modal and chemical variations in matrix. *Geochimica et Cosmochimica Acta* 43,

1761–1765.

Miyahara M., Yamaguchi A., Saitoh M., Fukimoto K., Sakai T., Ohfuji H., Tomioka N., Kodama Y., & Ohtani E. (2020). Systematic investigations of high-pressure polymorphs in shocked ordinary chondrites. *Meteoritics and Planetary Science*. doi: 10.1111/maps.13608.

Miyahara M. (2021) Aspect ratios and azimuth of chondrules in ordinary chondrites. doi.org/10.6084/m9.figshare.14060870

Nakamura T., Tomeoka K., Takaoka N., Sekine T., & Takeda H. (2000). Impact-induced textural changes of CV carbonaceous chondrites: Experimental reproduction. *Icarus* 146, 289–300.

Nelson V. & Rubin A.E. (2002). Size-frequency distributions of chondrules and chondrule fragments in LL3 chondrites: Implications for parent-body fragmentation of chondrules. *Meteoritics and Planetary Science* 37, 1361–1376.

Ohtani E., Kimura Y., Kimura M., Takata T., Kondo T., & Kubo T. (2004). Formation of high-pressure minerals in shocked L6 chondrite Yamato 791384: Constraints on shock conditions and parent body size. *Earth and Planetary Science Letters* 227, 505–515.

Ruzicka A.M., Hutson M., Friedrich J.M., Bland P.A., & Pugh R. (2015a). Northwest Africa 8709: A rare but revealing type 3 ordinary chondrite melt breccia. 78th Annual Meeting of the Meteoritical Society, 5348.pdf.

Ruzicka A.M., Grossman J., Bouvier A., Herd C.D.K., & Agee C.B. (2015b). *The Meteoritical Bulletin*, No. 101.

Sneyd D.S., McSween H.Y., Sugiura N., Strangway D.W., & Nord G.L. (1988). Origin of petrofabrics and magnetic anisotropy in ordinary chondrites. *Meteoritics* 23, 139–149.

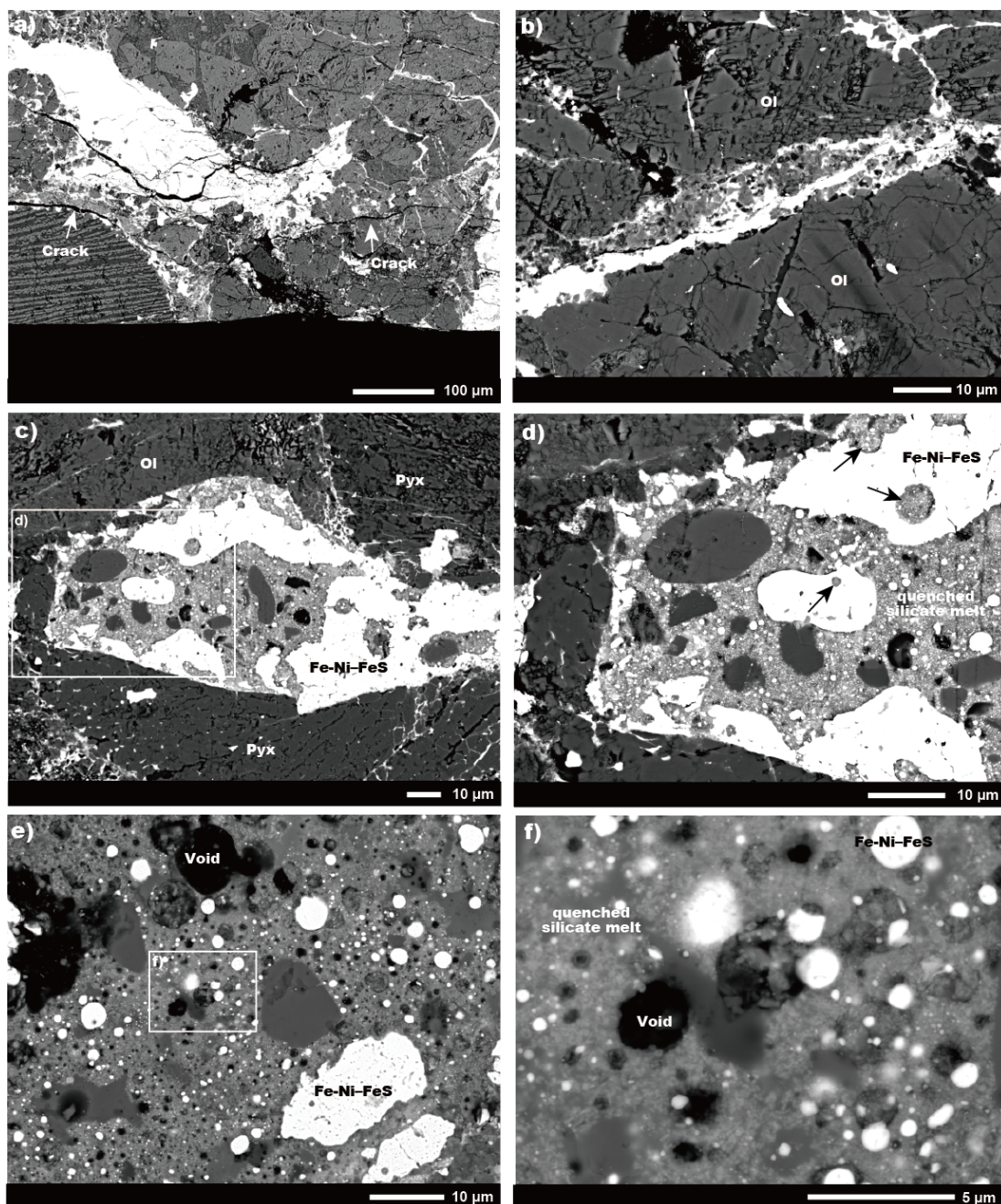
Stöffler D., Keil K., & Scott E.R.D. (1991). Shock metamorphism of ordinary chondrites. *Geochimica et Cosmochimica Acta* 55, 3845–3867.

Tanabata T., Shibaya T., Hori K., Ebana K., & Yano M. (2012). SmartGrain: High-throughput phenotyping software for measuring seed shape through image analysis. *Plant Physiology* 160, 1871–1880.

Tomeoka K., Yamahana Y., & Sekine T. (1999). Experimental shock metamorphism of the Murchison CM carbonaceous chondrite. *Geochimica et Cosmochimica Acta* 63, 3683–3703.

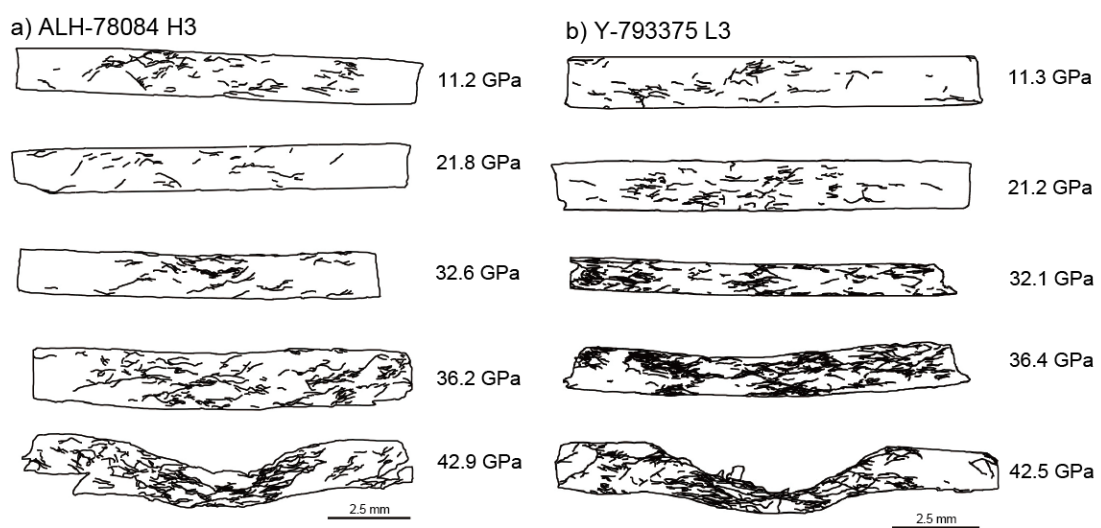
Trieloff M., Jessberger E.K., Herrwerth I., Hopp J., Fiéni C., Ghélis M., Bourot-Denise M., & Pellas P. (2003). Structure and thermal history of the H-chondrite parent asteroid revealed by thermochronometry. *Nature* 422, 502–506.

626 Weisberg M.K., McCoy T.J., & Krot A.N. (2006). Systematic and evolution of
 627 meteorite classification. In *Meteorites and the early solar system II* (e.d. by
 628 Lauretta and McSween), The university of Arizona Press, Tucson, pp19–52.
 629 Xie Z., Sharp T. G., & DeCarli P.S. (2006). High-pressure phases in a shock-induced
 630 melt vein of the Tenham L6 chondrite: Constraints on shock pressure and duration.
 631 *Geochimica et Cosmochimica Acta* 70, 504–515.
 632 Yamaguchi A. & Sekine T. (2000). Monomineralic mobilization of plagioclase by
 633 shock: an experimental study. *Earth and Planetary Science Letters* 175, 289–296.
 634



636 **Figure 1.** BSE images showing shocked ALH-78084 H3 chondrite. a) Open cracks
637 sub-parallel to a shockwave front (H_1_3). b) Planar or irregular cracks occurred in
638 some olivine grains (H_2_2), c) Melt between chondrules (H_3_3), d)
639 High-magnification image of a white-colored box in c). Mineral fragments entrained
640 into the melt were rounded. Metals include spherules of quenched silicate melt
641 (indicated by dark-colored arrows). e) Melt consisting of quenched silicate melts,
642 metals, mineral fragments, and voids (H_4_3), f) High-magnification image of a
643 white-colored box in e). Ol: olivine, Pyx: pyroxene, Fe-Ni: metallic Fe-Ni, FeS:
644 iron-sulfide.

645



646

647 **Figure 2.** Representative drawings of shocked samples. a) ALH-78084 H3 and b)
648 Y-793375 L3 chondrites. The upper direction is the impact surface.

649

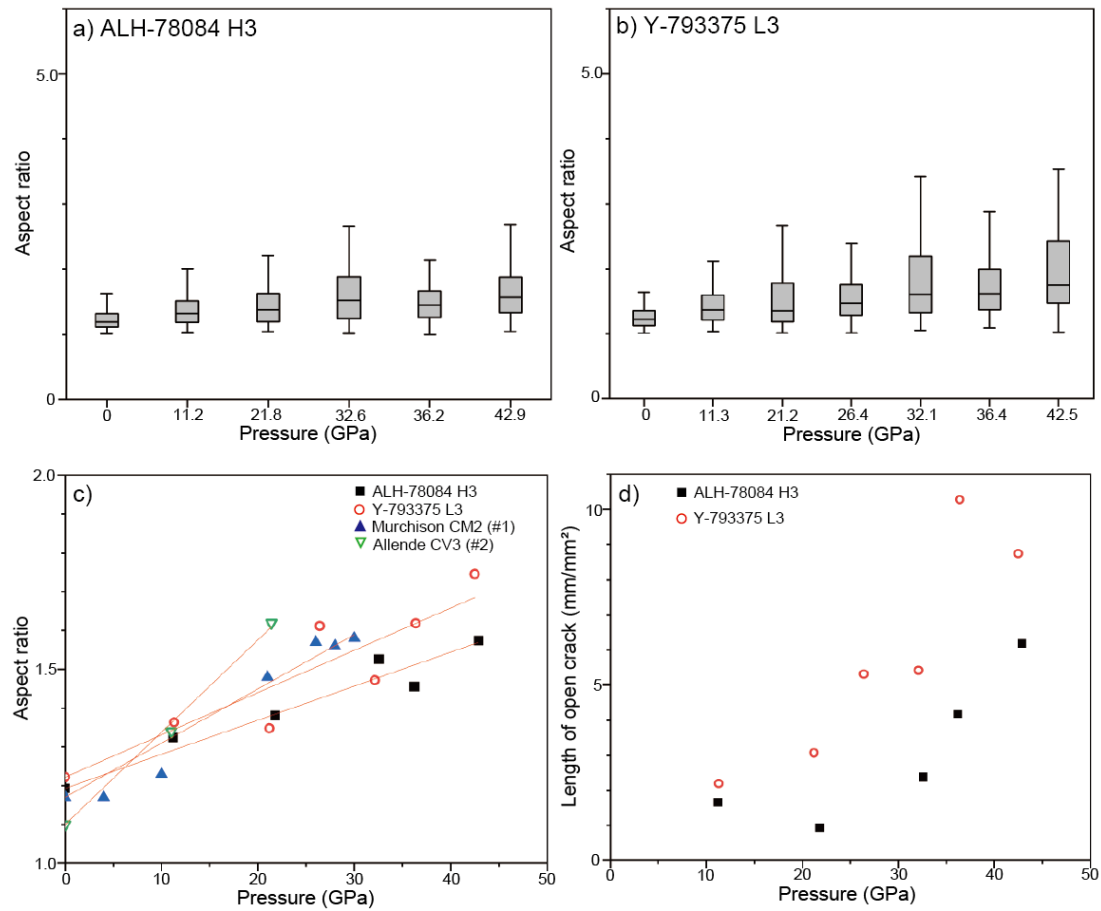


Figure 3. The morphological properties of chondrules. a) Relationship between shock pressure and the aspect ratios of chondrules. b) Relationship between shock pressure and the lengths of open cracks. #1 Tomeoka et al. (1999), #2 Nakamura et al. (2000)

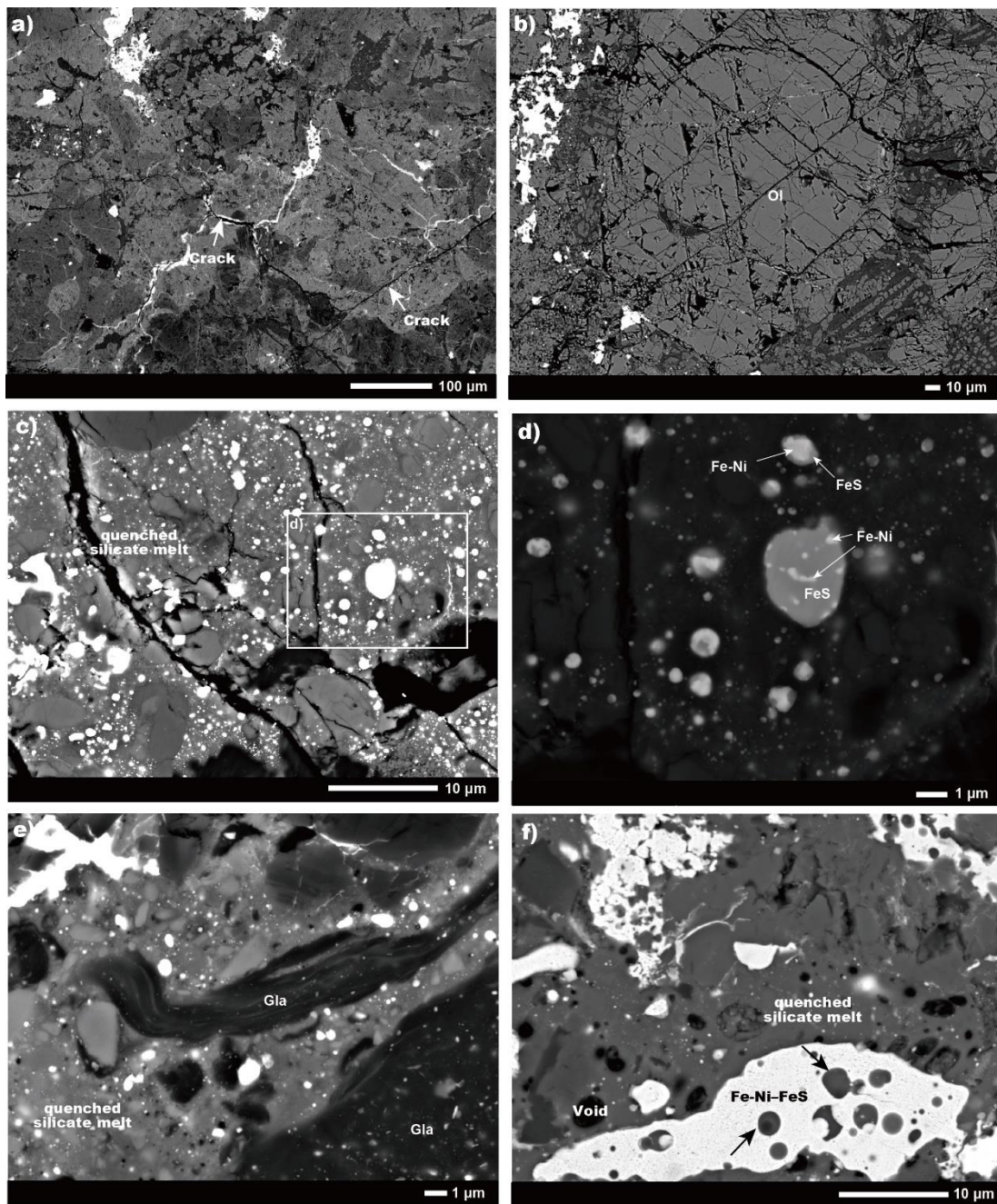


Figure 4. BSE images showing shocked Y-793375 L3 chondrite. a) Open cracks sub-parallel to a shockwave front (L_1_2), b) Planar- and irregular-fractures in some olivine grains (L_2_3), c) Melt between chondrules (L_2_3), d) High-magnification image of a white-colored box in c). The spherules of metallic Fe-Ni-FeS with a eutectic texture. e) Melted chondrule glasses in the melt (L_6_1). f) Metals including the spherules of quenched silicate melts (L_5_3). Ol: olivine, Pyx: pyroxene, Fe-Ni: metallic Fe-Ni, FeS: iron-sulfide, Gla: chondrule glass.

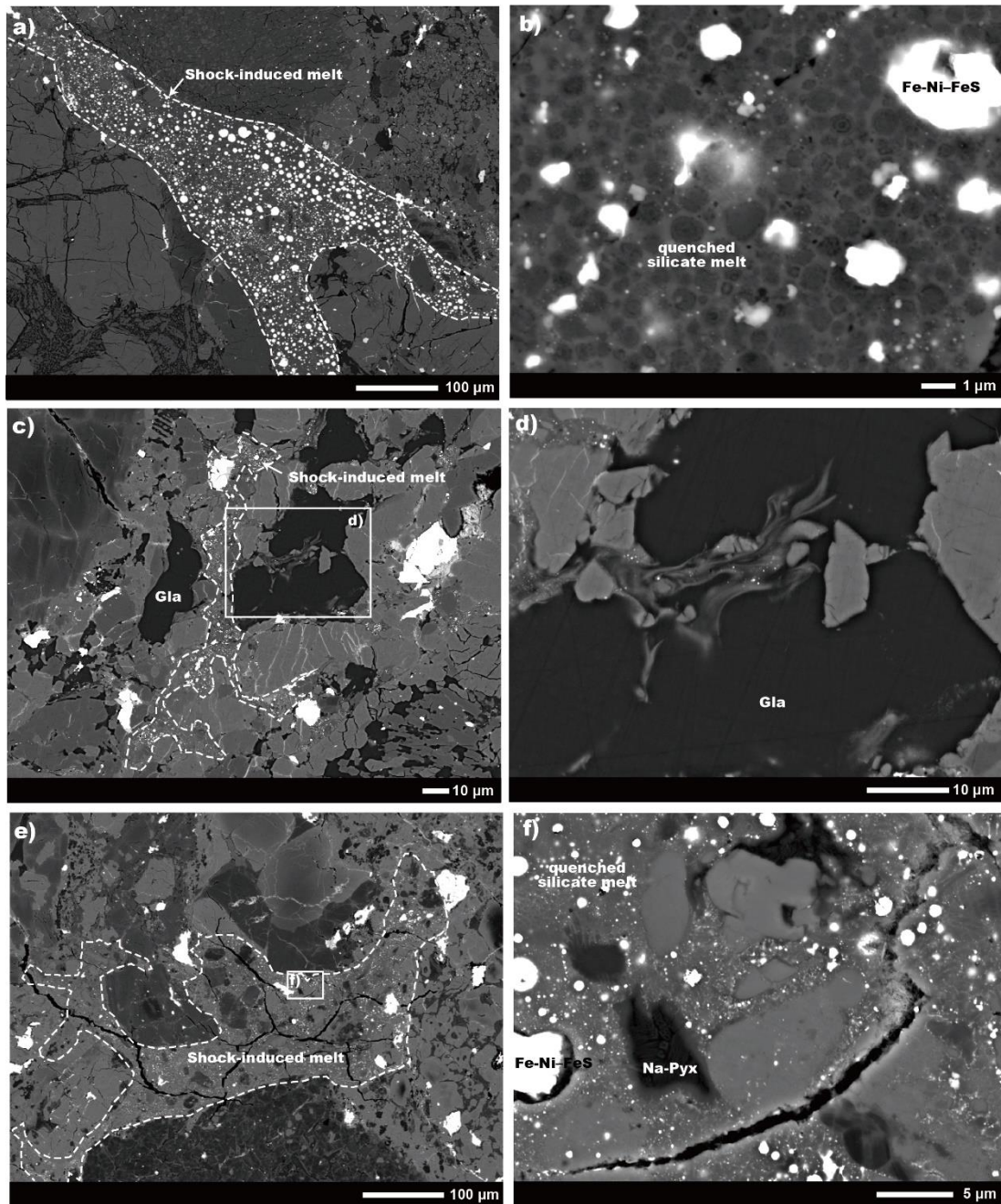
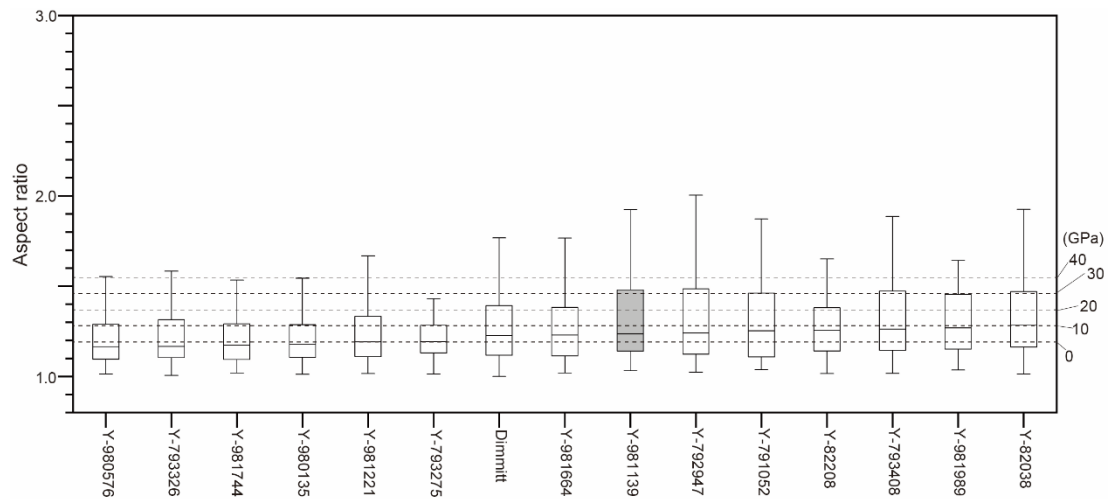


Figure 5. BSE images showing shock-induced melts in petrologic type 3 ordinary chondrites. a) Pocket type melt in the Aba Panu L3 chondrite. b) High-magnification image of shock-induced melt in a), c) Pocket type melt in A-87170 L3 chondrite, d) High-magnification image of a white-colored box in c). A flow-like texture appears in chondrule glasses, e) Pocket type melt in NWA 8664 L3 chondrite. f) High-magnification image of a white-colored box in e). Na-pyx: Na-pyroxene. Fe-Ni: metallic Fe-Ni, FeS: iron-sulfide.

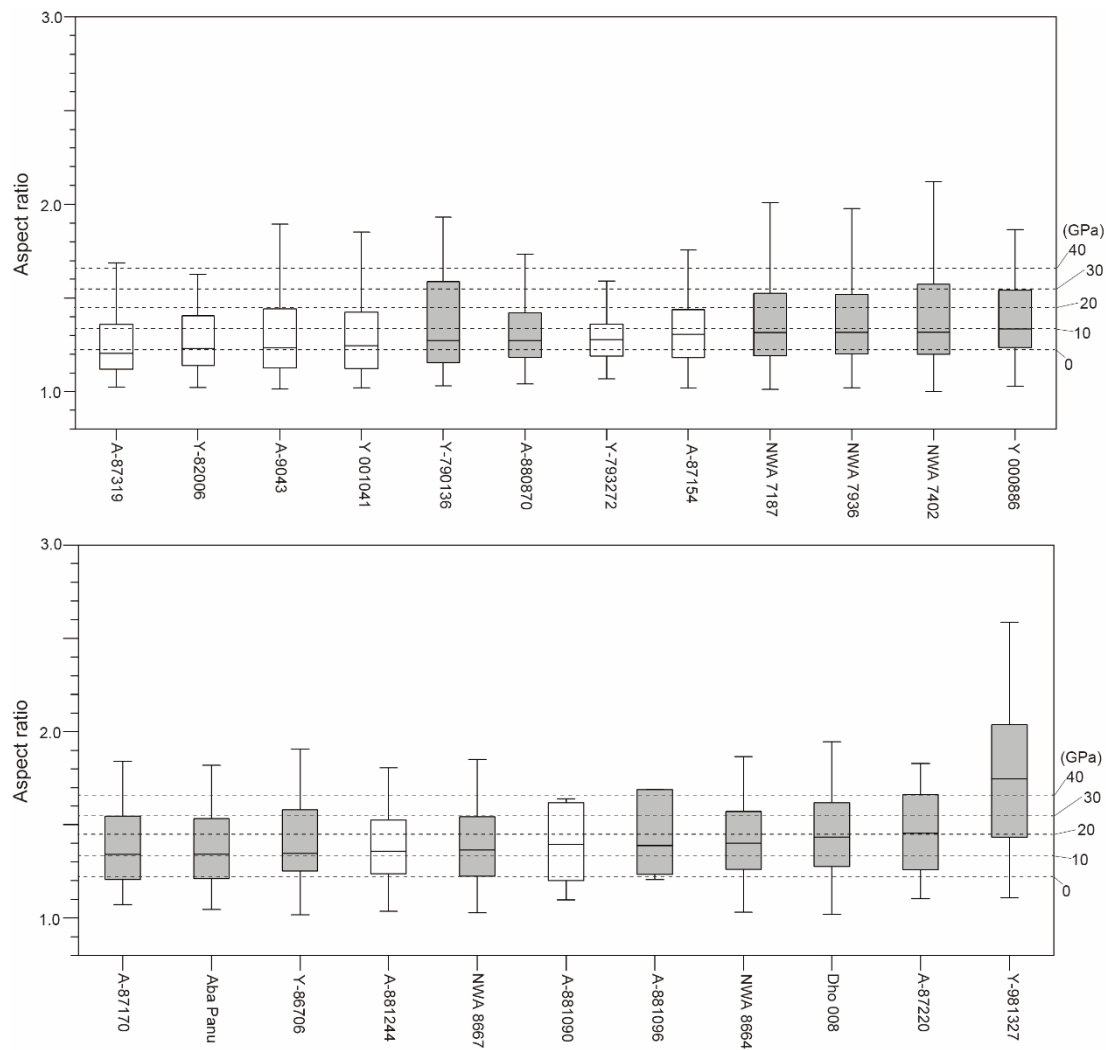


674

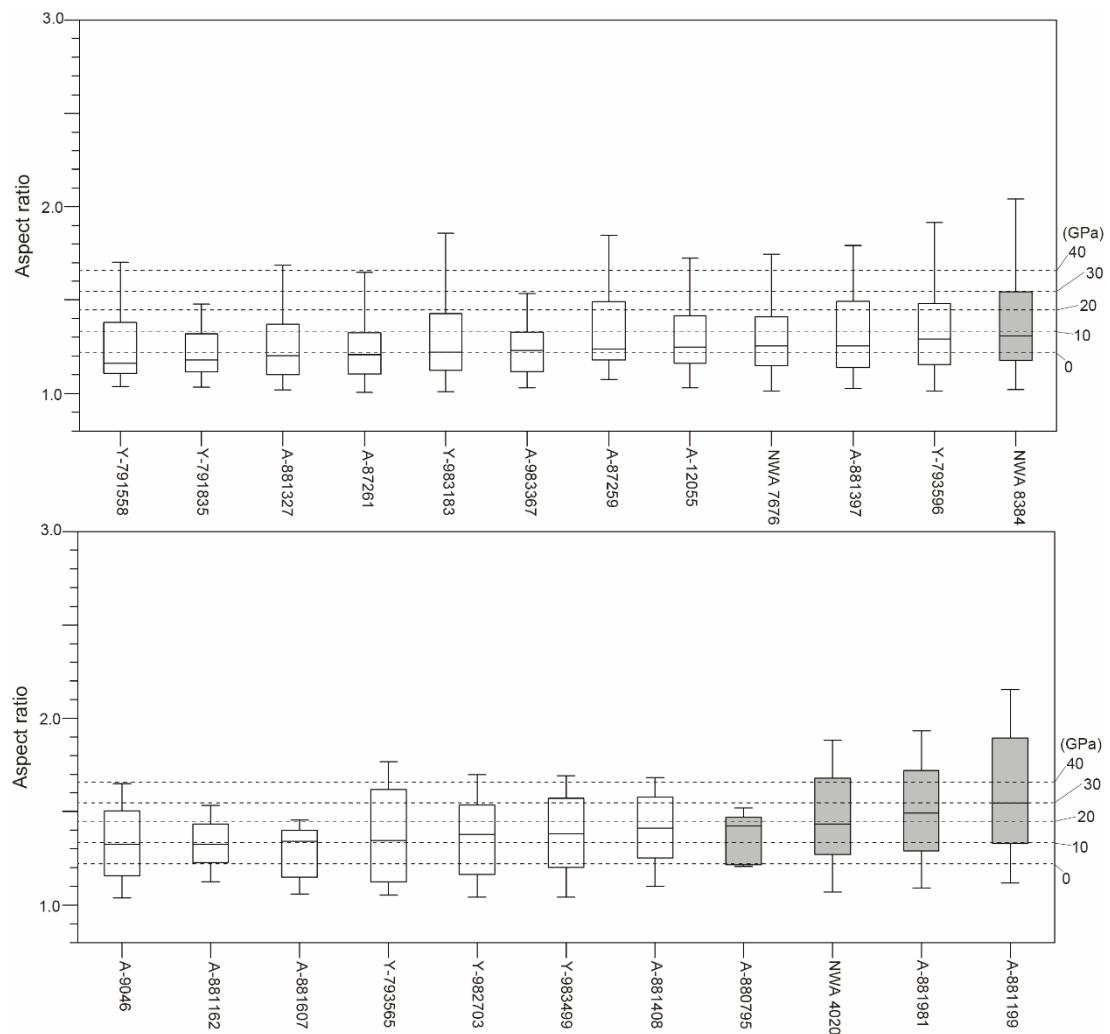
675 **Figure 6.** Box plots showing the aspect ratios of individual H3 ordinary chondrites.

676 The H3 ordinary chondrites are sorted according to the aspect ratios. White-colored
 677 and gray-colored boxes are H3 ordinary chondrites without melts and those with
 678 melts, respectively. Dashed lines correspond to each shock pressure estimated from
 679 the shock experiments of ALH-78084 H3 chondrite.

680



681
 682 **Figure 7.** Box plots showing the aspect ratios of individual L3 ordinary chondrites.
 683 The L3 ordinary chondrites are sorted according to the aspect ratios. White-colored
 684 and gray-colored boxes are L3 ordinary chondrites without melts and those with
 685 melts, respectively. Dashed lines correspond to each shock pressure estimated from
 686 the shock experiments of Y-793375 L3 chondrite.
 687



688

689 **Figure 8.** Box plots showing the aspect ratios of individual LL3 chondrites. The LL3
 690 ordinary chondrites are sorted according to the aspect ratios. White-colored and
 691 gray-colored boxes are LL3 ordinary chondrites without melts and those with melts,
 692 respectively. Dashed lines correspond to each shock pressure estimated from the
 693 shock experiments of Y-793375 L3 chondrite.

694 Table 1. Run table for shock experiments.

		Target				Flyer		Impact velocity (km/s)	Equilibrium pressure (GPa)	Sample recovery
		ϕ (mm)	Mass (g)	Thickness (mm)	Initial density (g/cm ³)	Material	Thickness (mm)			
ALH-78084 H3	H_1	12	0.554	1.51	3.24	SUS	2	0.57	11.2	Three slices
	H_2	12	0.543	1.49	3.18	SUS	2	1.03	21.8	Three slices
	H_3	12	0.563	1.52	3.30	SUS	2	1.46	32.6	Three slices
	H_4	12	0.564	1.50	3.30	SUS	2	1.59	36.2	Three slices
	H_5	12	0.544	1.49	3.19	-	-	-	-	Broken during preparation
	H_6	12	0.551	1.50	3.23	W	2	1.40	42.9	Three slices
	H_7	6	-	1.50	-	SUS	2	1.17	25.1	One disc
Y-793375 L3	L_1	12	0.536	1.49	3.14	SUS	2	0.57	11.3	Three slices
	L_2	12	0.542	1.49	3.18	SUS	2	1.01	21.2	Three slices
	L_3	12	0.536	1.52	3.14	SUS	2	1.44	32.1	Three slices
	L_4	12	0.580	1.49	3.40	SUS	2	1.22	26.4	Three slices
	L_5	12	0.577	1.47	3.38	SUS	2	1.60	36.4	Three slices
	L_6	12	0.589	1.49	3.45	W	2	1.38	42.5	Three slices

695 SUS: SUS 304, W: Tungsten

696

697

698 Table 2. Data table for recovered samples.

Shot No.		Shock pressure	Long axis ^{#2}	Short axis ^{#2}	Aspect ratio ^{#2}	Number of analyses	Length of open cracks	Gini coefficients
		(GPa)	(μm)	(μm)		<i>n</i>	(mm/mm ²)	
ALH-78084 H3	H_0 ^{#1}	0	429	352	1.19	258	-	0.33
	H_1	11.2	384	290	1.32	197	1.65	0.39
	H_2	21.8	414	273	1.38	162	0.93	0.46
	H_3	32.6	427	283	1.53	161	2.38	0.40
	H_4	36.2	389	254	1.46	187	4.17	0.41
	H_6	42.9	445	259	1.57	153	6.18	0.44
	H_7	25.1	-	-	-	-	-	-
Y-793375 L3	L_0 ^{#1}	0	773	634	1.22	143	-	0.32
	L_1	11.3	707	506	1.36	89	2.19	0.25
	L_2	21.2	634	393	1.35	115	3.07	0.23
	L_3	32.1	749	482	1.47	79	5.42	0.27
	L_4	26.4	1296	770	1.61	36	5.31	0.31
	L_5	36.4	821	507	1.62	83	10.28	0.31
	L_6	42.5	711	426	1.75	77	8.74	0.49

699 #1 Shot No. H_0 and L_0 are starting materials. #2 median values. H_5 is removed because it is lost. -: No data

700